Critical level interaction of a gravity wave with background winds driven by a large-scale wave perturbation

Mitsumu K. Ejiri,[1,2] Michael J. Taylor,[1] Takuji Nakamura,[3] and Steven J. Franke[4]

[1] As part of the Maui-Mesosphere and Lower Thermosphere program, data from the Utah State University Mesospheric Temperature Mapper (MTM) and the University of Illinois Meteor Wind Radar (MWR) have been used to investigate wave-driven dynamical interactions in the upper mesosphere at low latitudes. On 29 June 2003, short-period ($\sim$20 min) gravity waves (GWs) were imaged in the MTM in the near-infrared OH and O_2 airglow emissions for most of the night from 0700 to 1500 UT. The GWs were observed to disappear rapidly in the O_2 data (peak altitude: $\sim$94 km) around 1400 UT but remained evident in the lower altitudes OH data ($\sim$87 km) for a further 30 min. Coincident background wind variations measured by the MWR suggest that the GW disappearance at the O_2 layer was most probably caused by a critical level (CL) interaction. However, at the OH layer, the GW fading may also have been due to wave saturation and instabilities. During this period (1400$-$1500 UT), no significant change in OH and O_2 rotational temperatures were measured by the MTM; however, the background winds centered on the airglow layers were observed to increase by $\sim$10 m/s. The background wind acceleration from the disappearing gravity waves estimated from the airglow observations was larger below the CL than at the CL, consistent with the wind variation observed by the MWR.

Citation: Ejiri, M. K., M. J. Taylor, T. Nakamura, and S. J. Franke (2009), Critical level interaction of a gravity wave with background winds driven by a large-scale wave perturbation, *J. Geophys. Res.*, *114*, D18117, doi:10.1029/2008JD011381.

1. Introduction

[2] Atmospheric gravity waves (GWs), generated by sources in the troposphere and the lower stratosphere, propagate play a central role in governing the dynamical coupling between the lower and upper atmospheric regions [*Reid*, 1986]. GWs propagate energy upward and eventually dissipate through one of several mechanisms, depositing their momentum and energy in the background wind and temperature fields. In particular, small-scale GWs with periods of <1 h have been shown to be responsible for as much as 70% of the wave-induced transport that occurs in the mesosphere and lower thermosphere (MLT) region [*Fritts and Vincent*, 1987], although gravity waves with periods >1 h are also important [*Nakamura et al.*, 1993].

[3] Radar and lidar techniques have been used to investigate GW, frequencies, amplitudes, vertical structures, and flux's averaged over various time intervals [e.g., *Reid*, 1986; *Nakamura et al.*, 1993; *She et al.*, 1991; *Hecht et al.*, 1993].

[1]Center for Atmospheric and Space Sciences and Physics Department, Utah State University, Logan, Utah, USA.
[2]Now at Research Institute for Sustainable Humanosphere, Kyoto University, Uji, Japan.
[3]Research Institute for Sustainable Humanosphere, Kyoto University, Uji, Japan.
[4]Department of Electrical and Computer Engineering, University of Illinois at Urbana-Champaign, Urbana, Illinois, USA.

Horizontal scales and parameters of GWs have been estimated by multiradar observations [e.g., *Meek and Manson*, 1992; *Gavrilov et al.*, 1995]. However, radar information on the horizontal dynamics of GWs has been limited. On the other hand, airglow imaging techniques have been used to determine the horizontal structures of GWs that modulate the airglow emission layers that reside in the MLT region and also to quantify their momentum flux (F_M) for vertically propagating waves [*Swenson and Liu*, 1998]. Previous statistical studies of GWs observed by airglow imagers have reported typical spatial and temporal scales of 5 to 60 km and 5 to 30 min for the horizontal wavelengths and observed periods, respectively [e.g., *Wu and Killeen*, 1996; *Taylor et al.*, 1997; *Walterscheid et al.*, 1999; *Ejiri et al.*, 2003; *Nakamura et al.*, 1999, 2001, 2003; *Suzuki et al.*, 2004; *Wrasse et al.*, 2006]. Recently, several attempts have been made to estimate the F_M carried by gravity waves seen in airglow images [*Swenson and Liu*, 1998; *Gardner et al.*, 1999; *Fritts et al.*, 2002; *Hickey and Brown*, 2002; *Tang et al.*, 2002, 2005; *Espy et al.*, 2004; *Suzuki et al.*, 2007]. In particular, *Yamada et al.* [2001] reported a breaking GW event observed with an OH imager exhibiting very large intensity perturbations ($I'/\bar{I} \sim 55\%$). *Fritts et al.* [2002] estimated that this event had an extremely large F_M of $\sim$900 m²/s² and produced a mean flow acceleration of $\sim$80 m/s in less than an hour. In contrast, *Hickey and Brown* [2002] determined the altitude variation of F_M using ALOHA-93 GW parameters observed in O_2 atmospheric band and OI (557.7 nm) combined with modeling. They

analyzed four more typical GW events and found that only one had a maximum $F_M > 50$ m^2/s^2. Indeed, most waves (over 90%) evident in midlatitude airglow imagery carry relatively small amounts of F_M (less than 10 m^2/s^2) [*Tang et al.*, 2005]. and large F_M events appear to relatively rare.

[4] Strong wind shears associated with the GWs may be large enough to create dynamical instabilities in the form of Kelvin-Helmholtz (KH) billows. Similarly, the background temperature gradient could be large enough to form a convective instability, or the wave may encounter a critical level at which the horizontal phase velocity relative to the ground equals the background wind velocity. Even in the absence of instabilities, GWs may be absorbed into the mean flow through viscous dissipation. Although features suggesting dynamical instabilities have long been known to exist in the mesosphere [e.g., *Lloyd et al.*, 1973], only recently, with the advent of advanced numerical models, lidars, radars, and airglow imagers, have more definitive studies been possible. Many researchers have examined the structures formed when dynamical instabilities occur [e.g., *Lloyd et al.*, 1973; *Gossard and Hooke*, 1975; *Reid et al.*, 1987; *Fritts et al.*, 1997]. In the simplest situation of a speed shear (no rotational shear), dynamical instability structures can form that are aligned parallel to the phase front of the GW and perpendicular to the direction of the shear. Several studies have also examined convective instabilities produced by breaking GWs. In particular, *Fritts et al.* [1997] used a three-dimensional numerical simulation to show that the phase fronts produced by a convective instability are aligned perpendicular to the breaking GW crests. *Hecht et al.* [1997, 2000] have described observations of such perpendicular wave-like structures in the OH emission at the same time when lidar observations of the temperature gradient (from 85 to 90 km) indicated the presence of a super adiabatic lapse rate.

[5] The importance of critical levels (CL) in the dynamics of the atmosphere has been long recognized [e.g., *Bretherton*, 1966; *Booker and Bretherton*, 1967; *Hazel*, 1967; *Hines*, 1968; *Breeding*, 1971; *Gossard and Hooke*, 1975; *Taylor et al.*, 1993; *Huang et al.*, 1998; *Gardner and Taylor*, 1998]. In the simplest case, as the GW approaches a CL, its vertical wavelength decreases, coming close to zero at the CL, the point at which the wave can no longer propagate vertically. Subsequent wave dissipation at a CL can cause large accelerations of the mean flow. When a vertically propagating GW approaches a CL perturbations of horizontal wind associated with the GW (GW amplitude) increase significantly with altitude. The GW becomes saturated at an altitude where its amplitude becomes equal to its intrinsic phase speed. This altitude is called the saturation level (SL). *Fritts* [1984] has discussed the mean flow acceleration caused by GW dissipation between the saturation level and the critical level. For example, a model study by *Hickey and Brown* [2002] using a GW event measured during the ALOHA-93 campaign showed that the wave momentum flux (F_M) decreased rapidly with increasing height from ~64 m^2/s^2 at 92 km to 0 m^2/s^2 at 94 km as a consequence of the critical level interaction. The expected mean flow acceleration associated with this F_M divergence reached a value of 200 m/s/h just below the critical level. *Hecht et al.* [2001] used medium-frequency (MF) radar to determine wind acceleration in association with small-scale features in airglow image data generated by a

dynamical instability. They concluded that the acceleration event was due to a CL-GW interaction. *Huang et al.* [1998, 2002] observed a sudden and large mesospheric heating (peak temperature rise ~40 K) using Na wind/temperature lidar measurements during the ALOHA-93 campaign. They compared GWs observed by an airborne airglow imager [*Swenson et al.*, 1995] with the lidar wind and temperature profiles [*Tao and Gardner*, 1995] and concluded that the temperature increase was caused by heating due to turbulence in the background medium resulting from shear instability induced by a CL-GW interaction. However, the evidence for this interaction was indirect in these studies.

[6] In this study, we present new observations of a short-period GW event observed in two MLT airglow emissions, together with background wind and temperature measurements recorded simultaneously over Maui, Hawaii, on 29 June 2003. A detailed investigation of these joint data sets demonstrates more directly that the GWs dissipated during a CL-GW interaction. We further suggest that a significant portion of the observed background wind field acceleration was caused by deposition of the gravity wave momentum flux at the CL and below.

2.   Instrumentation and Observations

[7] The Maui-Mesosphere and Lower Thermosphere (MALT) program utilized an optical and radar instrumentation suite to investigate the dynamics of the low-latitude middle atmosphere in unprecedented detail. This program was a joint research initiative between the U.S. Air Force Office of Scientific Research (AFOSR) and the National Science Foundation (NSF), utilizing the Air Force Maui Optical Station (AMOS) facility at the summit of Haleakala Crater, Maui, Hawaii (20.8°N, 156.2°W). As part of this program, the Utah State University Mesospheric Temperature Mapper (MTM) was operated at this site for a 5-year period (November 2001 to December 2006), providing two-dimensional airglow intensity and rotational temperature measurements. From May 2002, these measurements were complemented by continuous observations of the MLT wind field (~80–100 km) using the University of Illinois Meteor Wind Radar (MWR) located at Kihei, Maui, Hawaii (20.8°N, 156.4°W). Together these data have enabled detailed investigations of short-period gravity waves.

2.1.   Mesospheric Temperature Mapper

[8] The MTM is a high-performance imaging system capable of observing wave-induced fluctuations in intensity and rotational temperatures for the OH(6,2) Meinel band and $O_2(0,1)$ atmospheric band emissions. A large-format (6.45 cm^2), 1024 × 1024 pixel CCD array is coupled to a telecentric lens system with a circular field of view of 90°. The high quantum efficiency and low noise characteristics of the CCD array provide precise measurements of OH and O_2 emission intensity (<0.5% in 1 min) and derived rotational temperatures (<1–2 K in 3 min) [e.g., *Pendleton et al.*, 2000; *Taylor et al.*, 2001].

[9] Sequential exposures were made using temperature-stabilized narrow-band ($\Delta\lambda \sim 1.2$ nm) filters centered at 840 and 846.5 nm for the OH(6,2) Meinel band ($P_1(2)$ and $P_1(4)$, respectively) and 866 and 868 nm for the $O_2(0,1)$ atmospheric band, followed by a background sky measurement
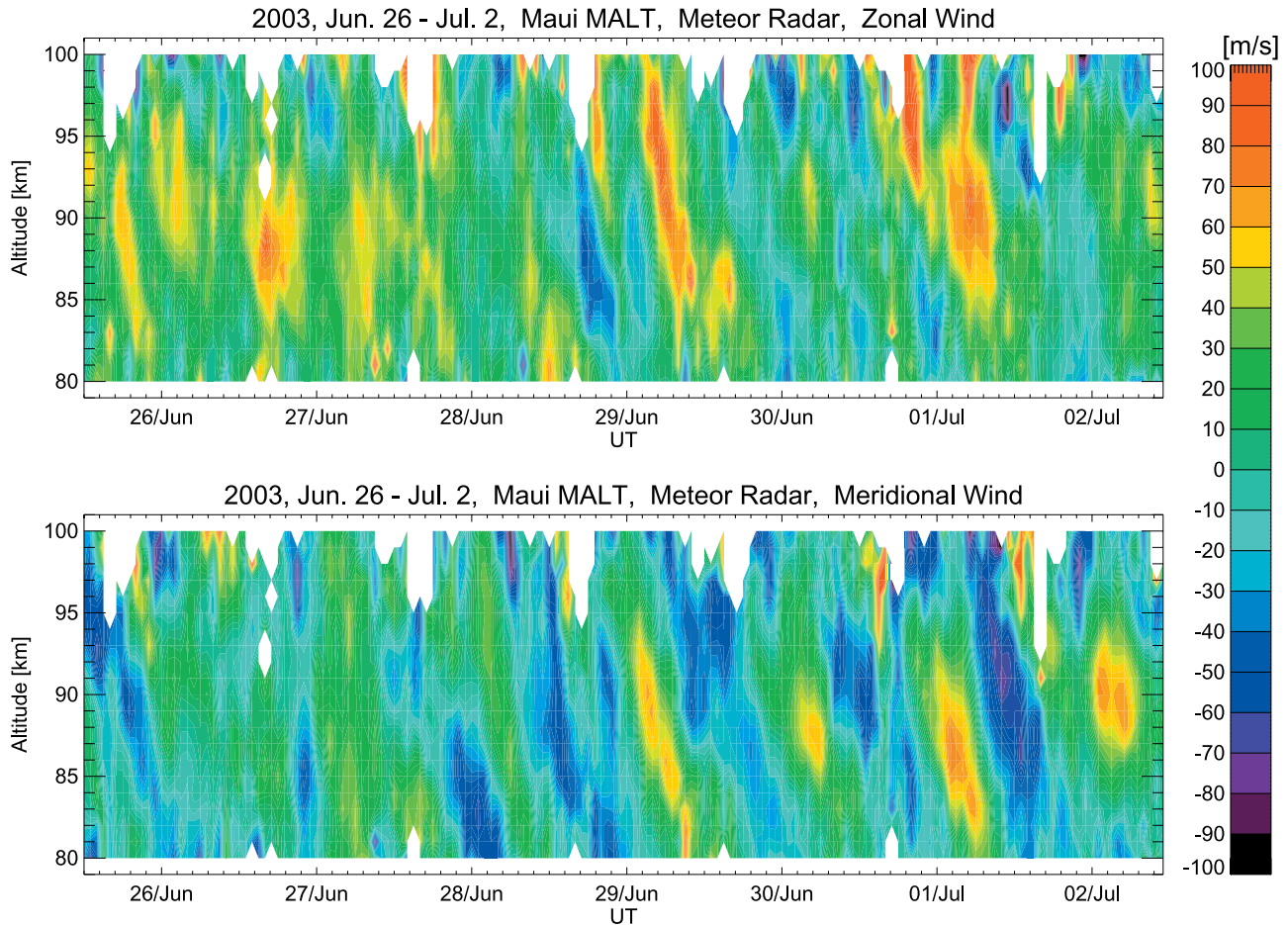
Figure 1. (top) Zonal and (bottom) meridional wind over Maui as measured by the MWR during a 7-day period (26 June to 2 July 2003).

at 857 nm. The exposure time for each filter was 60 s, resulting in a cycle time of ∼5.5 min. Zenith rotational temperatures were computed separately for both emissions using the ratio method, as described by *Meriwether* [1984], and have been compared directly with simultaneous temperature measurements obtained by the University of Illinois wind-temperature lidar as part of the Maui-MALT program. Nocturnal temperature variability measured by these two different instrumental techniques showed good agreement with average root-mean squares of temperature differences of approximately 6 to 7 K at the assumed emission altitudes of 87 km (OH) and 94 km (O_2) [*Zhao et al.*, 2005].

2.2. Meteor Wind Radar

[10] The University of Illinois MWR is a commercially available SKiYMET system operated at 40.92 MHz, and has been described in detail by *Franke et al.* [2005]. The algorithms used to compute the meteor trail position and Doppler shift have also been fully described by *Hocking and Thayaparan* [1997]. Wind velocities were estimated from the trail positions and Doppler shifts using a weighted least squares fit to an assumed constant wind vector composed of horizontal eastward and northward components (with negligible vertical wind component). The height resolution of the estimated winds was 4 km. Processed zonal and meridional wind profiles are readily available at

1-km intervals with a time resolution of 30 min throughout the 80 to 100 km range.

[11] Figure 1 shows an example of the zonal and meridional wind fields over Maui measured by the MWR during a 7-day period (26 June to 2 July 2003), plotted with height and time resolutions of 4 km and 1 h, respectively. The wind field during this time was dominated by an ∼24-h-period oscillation with a clear downward phase progression of ∼1 km/h, most probably due to the diurnal tide. On 29 June, this tidal signature was particularly strong in both the zonal and meridional wind components. A critical level event for a short-period (∼20 min) gravity wave was observed on this night, as detailed in sections 3 and 4.

3. Analysis

3.1. Image Processing and Wave Parameter Analysis

[12] To investigate GWs, the MTM images were processed using the following procedure. First, the images were calibrated using the star field and then bright pixels due to stars (or cosmic rays) were replaced by average values of the surrounding pixels. Each image was then flat-fielded using the nightly average intensity. OH (O_2) rotational temperatures were calculated from the sequential $P_1(2)$, $P_1(4)$ (866 nm, 868 nm) and background image, and then their corresponding band intensities were determined. The
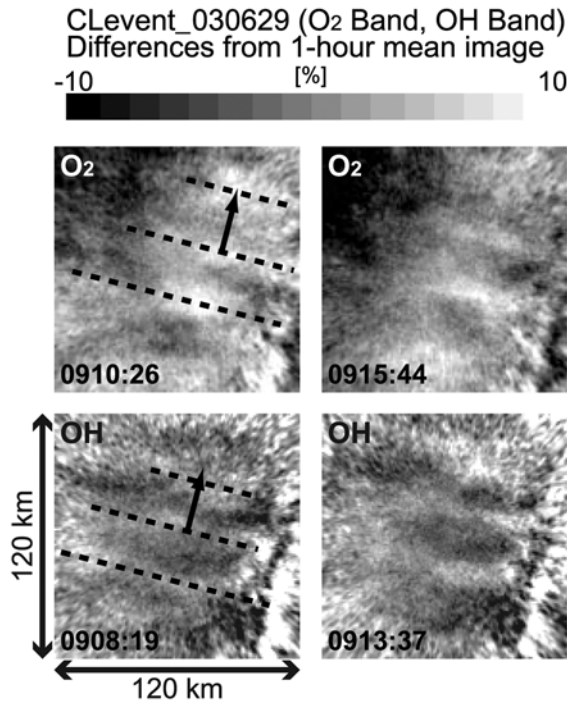
Figure 2. Short-period (~20-min) GWs obtained in the processed (bottom) OH band and (top) O_2 band intensity images around 0910 UT on 29 June 2003. These images are shown as differences (in percent) from a 1-h average image. Each image represents a 120-km-square area at the airglow altitudes (OH: 87 km, O_2: 94 km). Upward and to the right are north and east, respectively. The GW wavefront and horizontal propagation direction are marked with a dashed line and arrow, respectively.

processed images were then transformed into geographical coordinates and for this study plotted on a linear scale of 120 by 120 km. The mapped data were then analyzed to determine the horizontal parameters of observed GWs using well-developed three-dimensional fast Fourier transform (FFT) [e.g., *Garcia et al.*, 1997; *Coble et al.*, 1998], and their observed phase speeds were obtained by comparing wavefront positions using a time sequence of mapped images.

3.2. Momentum Flux

[13] *Swenson and Liu* [1998] developed a method for estimating momentum flux (F_M) associated with a freely propagating gravity wave using its perturbation amplitude ($I'/\bar{I}$), observed in the OH emission and its intrinsic wave parameter measurements (i.e., as measured in a reference frame moving with the background wind). Their formulation was derived under the assumption that the GW horizontal wavelength (λ_h) is much larger than its vertical wavelength (λ_z) in the MLT region. Owing to the finite depth of the OH and O_2 emission layers (full width at half maximum (FWHM) of typically 8–10 km), only gravity waves with λ_z significantly greater than the layer depth will be readily observed in the image data. Our estimates of λ_z associated with short-period GWs indicate values comparable to their observed horizontal wavelengths (typically >20 km). We have there-

fore revised the formula developed by *Swenson and Liu* [1998] under the assumption of $\lambda_z \sim \lambda_h$. The vertical group velocity (V_{gz}) can then be described as follows [*Vincent*, 1984]:

$$V_{gz} = -\frac{m}{(m^2 + k^2)}\frac{\omega^2 - f^2}{\omega^2}, \qquad (1)$$

where ω is the intrinsic frequency, f is the inertial frequency, and k ($= 2\pi/\lambda_h$) and m ($= 2\pi/\lambda_z$) are the horizontal and vertical wave numbers, respectively. We then obtain a relationship between momentum flux, F_M, and airglow intensity perturbation, I',

$$F_M = \frac{mk}{(m^2 + k^2)}\frac{g^2}{N^2(\mathrm{CF})^2}\left(\frac{I'}{\bar{I}}\right)^2, \qquad (2)$$

where N and g are the Brunt-Väisälä frequency (typically = 2.0×10^{-2} rad/s) and gravity acceleration (= 9.5 m/s^2), respectively. CF is the cancellation factor relating the airglow intensity to the wave-perturbed atmospheric temperature and the observed intensity perturbation of the GW to its vertical wavelength [*Swenson and Liu*, 1998; *Vargas et al.*, 2007]. To avoid strong cancellation effects within the airglow, CF is usually calculated for $\lambda_z > 10$ km, which is the practical limit for observing short-period GW. Note that uncertainties in CF for $\lambda_z < 20$ km can lead to large uncertainties in F_M, especially when λ_z is close to 10 km (CF < 1). The vertical wave number m is estimated for each wave event using the simplified GW dispersion relation, assuming that the atmosphere is an adiabatic incompressible fluid [*Hines*, 1960],

$$m^2 = \frac{N^2}{(c-u)^2} - \frac{1}{4H^2} - k^2, \qquad (3)$$

where H is a scale height (typically ~6 km), c is the observed GW horizontal phase speed, and u is the background wind velocity projected in the direction of horizontal wave propagation. The background winds were height-averaged using a Gaussian weighting with a FWHM of 5.6 km (5.5 km) for OH (O_2) applied to the MWR data centered at 87 ± 3 km (94 ± 3 km) for OH (O_2).

4. Results

[14] On 29 June 2003 the MTM was operated from 0700 to 1500 UT. Short-period (~20 min) GWs were observed in both the OH and O_2 airglow layers almost continuously during this night from ~0800 to 1400 UT. Figure 2 shows the GWs evident in the processed OH band (Figure 2, bottom) and O_2 band (Figure 2, top) intensity data at ~0910 UT. To highlight the wave structures the images are shown as differences (in percent) from a 1-h average image, plotted on a linear scale 120 by 120 km. The top and right of each image are north and east, respectively. The GW wavefront and horizontal propagation direction are indicated by the dashed lines and arrows, respectively. In both the O_2 and OH data the GWs propagated from SSW to NNE with similar horizontal wavelengths and phase velocities of 23.5 km and 23.5 m/s for O_2 and 24.5 km and 19.0 m/s
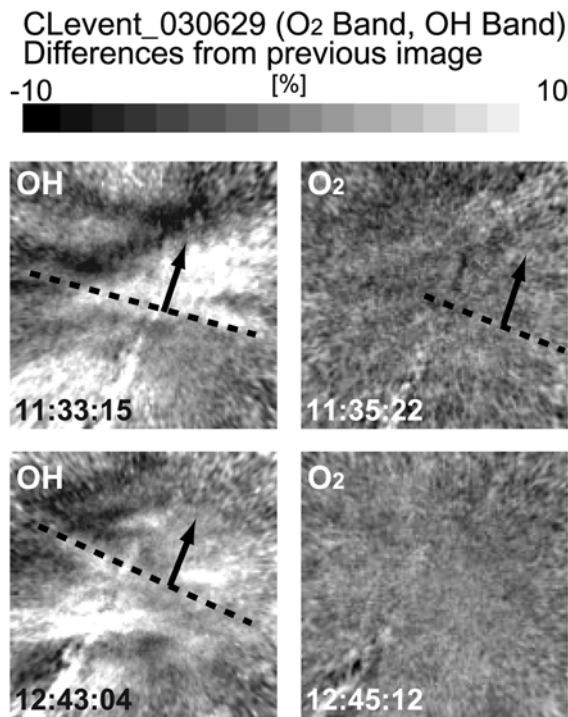
Figure 3. Typical GW structure observed in the (left) OH and (right) O_2 images at (top) 1100 UT and (bottom) 1200 UT on 29 June 2003. These images are shown as differences (in percent) from a 1-h average image. The GW wavefront and horizontal propagation direction are marked with a dashed line and arrow, respectively. The GWs in OH images are clearly seen at both 1100 and 1200 UT, while the GW structures in O_2 images are unclear at 1100 UT and absent at 1200 UT.

for OH, respectively. This wave pattern was evident in both emission layers for over 7 h, except for $1100-1300$ UT in O_2.

[15] The GWs in the O_2 data were observed continuously from 0800 to 1100 UT, after which time the wave structure grew faint and the horizontal parameters could no longer be defined (as shown in Figure 3, top right). No O_2 wave structure was recognized after $\sim$1200 UT (Figure 3, bottom right). However, this event reappeared around 1300 UT and was evident for a further $\sim$1 h before fading rapidly around 1400 UT, as shown in the image time sequence of Figure 4. In particular, the GW (delineated by the dashed lines) was still visible at 1401 UT (Figure 4, 14:01:21 image) but had disappeared by 1406 UT (Figure 4, 14:12:59 image). Comparison with the OH data shows that this GW event was observed continuously from 0700 to 1430 UT (including the period $1100-1300$ UT, when the O_2 wave structure had faded), thereafter it also disappeared. This is shown in Figure 5, where the GW crests (dashed lines) can be seen clearly at 1416 UT but by $\sim$1430 UT the pattern had faded and the horizontal wavelength had decreased. The GW continued to fade and disappeared around 1445 UT.

5. Discussion

[16] The GWs disappeared first in the O_2 image data, and then in the OH image data 30 min later, as presented in Figures 3, 4,
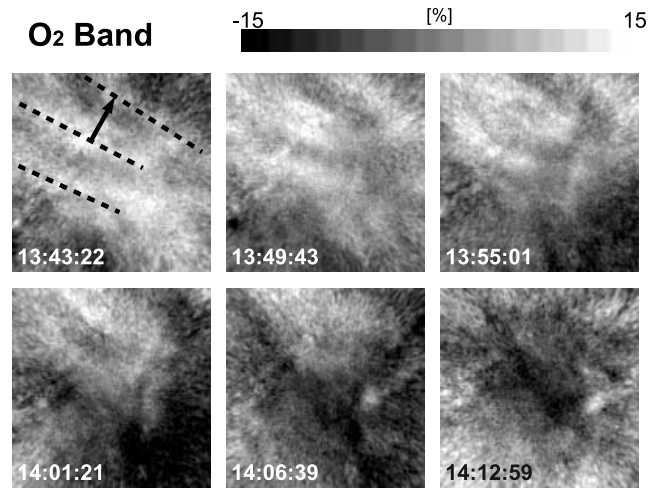

Figure 4. The disappearance of GWs from the O_2 images around 1400 UT. These images are shown as differences (in percent) from a 1-h average image with a time interval of $\sim$6 min. In the 13:43:22 image the GW wavefront and horizontal propagation direction are marked with a dashed line and arrow, respectively. The GW can be seen by 1401 UT (14:01:21 image) but disappears at 1406 UT (14:06:39 image).

and 5. The GW in the O_2 data disappeared immediately after 1401 UT (Figure 4). The GW in the OH data first grew faint and then disappeared (Figure 5). It is notable that the wavelength became shorter (similar to an instability event) at $\sim$1430 UT and faded after 1439 UT. To investigate the disappearances, temporal variations in their propagation parameters and background winds have been analyzed in detail.

[17] Table 1 summarizes the horizontal parameters of the GW for each emission as measured at hourly intervals from 0700 to 1400 UT. The temporal variations in the
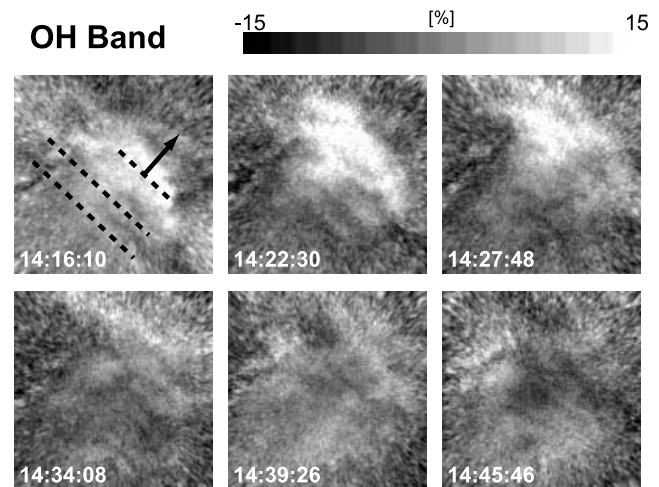

Figure 5. The image format follows Figure 4 for the OH images around 1430 UT. The GW can be seen clearly by 1422 UT (14:22:30 image). The wavelength became shorter at $\sim$1430 (14:27:48 and 14:34:08 images). The GW then fades (14:39:26 image) and disappears after 1445 UT (14:45:46 image).
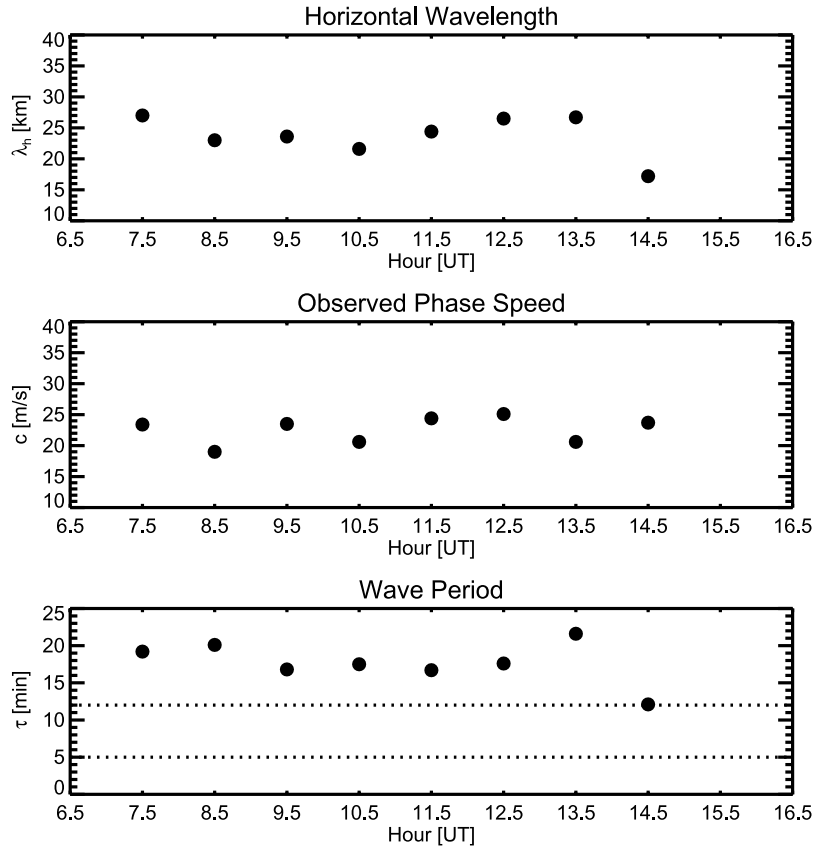
Figure 6. GW propagation parameter temporal variations obtained in the OH images: (top) horizontal wavelengths (λ_h, standard deviation error: 1–1.5 km), (middle) horizontal phase speeds (c, standard deviation error: 0.5–1.5 m/s), and (bottom) observed periods (τ, standard deviation error: 0.5–1.5 min). In the bottom plot, two dotted lines show 5-min and 12-min lines as a typical Brunt-Väisälä period (lower line) and twice the observation sequence (upper line), respectively.

OH parameters: horizontal wavelength (λ_h, Figure 6, top), observed horizontal phase velocity (c, Figure 6, middle), and observed wave period (τ, Figure 6, bottom) are shown. The two dotted lines in Figure 6 (bottom) indicate the Brunt-Väisälä period, ~5 min, and the Nyquist period ~12 min. These wave parameters were almost constant during the night up until 1430 UT with standard deviations for λ_h, c, and τ of only 2 km, 2 m/s, and 2 min, respectively. The λ_h and τ at 1430 UT were significantly smaller than those before 1330 UT because the wavelength became shorter at ~1430 UT.

[18] Figure 7 (top) shows vectors representing the speed and direction of the GW imaged by the MTM in the O_2 emission during the period from 0600 to 1600 UT on 29 June 2003. No arrow indicates that the GWs were absent (or insufficiently clear to determine the wave propagation parameters) from the image data. Corresponding background wind vectors at the nominal O_2 emission altitude are also shown. The background winds were averaged with a Gaussian weighting in altitude with a FWHM of 5.5 km using the MWR wind data centered at 94 ± 3 km for O_2 data. Figure 7 (bottom) plots the corresponding wave and wind measurements for the OH data using a Gaussian weighting for the wind data of 5.6 km (FWHM) centered at 87 ± 3 km. The GW signatures in both the OH and O_2 layers were mainly directed toward the NNE throughout the night with speeds of approximately 19 to 28.5 m/s. In contrast, the direction

and magnitude of the background wind field varied significantly during the night at both the OH and O_2 layers. The meridional components of background winds changed from south to north around 1000 to 1100 UT at the O_2 layer and 1300 to 1400 UT at the OH layer. Zonal components of background wind increased eastward after 1400 UT at the O_2 layer and after 1100 UT at the OH layer. As a result, the background wind directions approached the GW propagation directions creating potential critical level (CL) conditions.

Table 1. Typical Values of GW Horizontal Propagation Parameters Observed at Each Hour[a]

| | Parameters | UT | | | | | | | |
		0700	0800	0900	1000	1100	1200	1300	1400
OH	λ_h (km)	27.0	23.0	23.5	21.5	24.5	26.5	26.5	17.0
	c (m/s)	23.5	19.0	23.5	20.5	24.5	25.0	20.5	23.5
	τ (min)	19	20	17	17.5	16.5	17.5	21.5	12
	Direction (°)	18	12.5	11.5	9	9	21	41.5	41.5
	I'/I (%)	2.5	3.8	2.1	3.4	3.0	2.3	3.6	3.1
O_2	λ_h (km)		27.0	24.5	26.0			27.5	
	c (m/s)		28.5	19.0	24.0			27.0	
	τ (min)		16	21.5	18			17.0	
	Direction (°)		42.5	19.5	6			39	
	I'/I (%)		3.4	2.7	3.2			3.9	

[a]Error of λ_h: $\pm 1 - 1.5$ km; error of c: $\pm 0.5\_1.5$ m/s; error of τ: $\pm 0.5 - 1.5$ min; error of direction: $\pm 1.5 - 2.5$ degree; and error of I'/I: $\pm 0.3 - 0.65\%$.
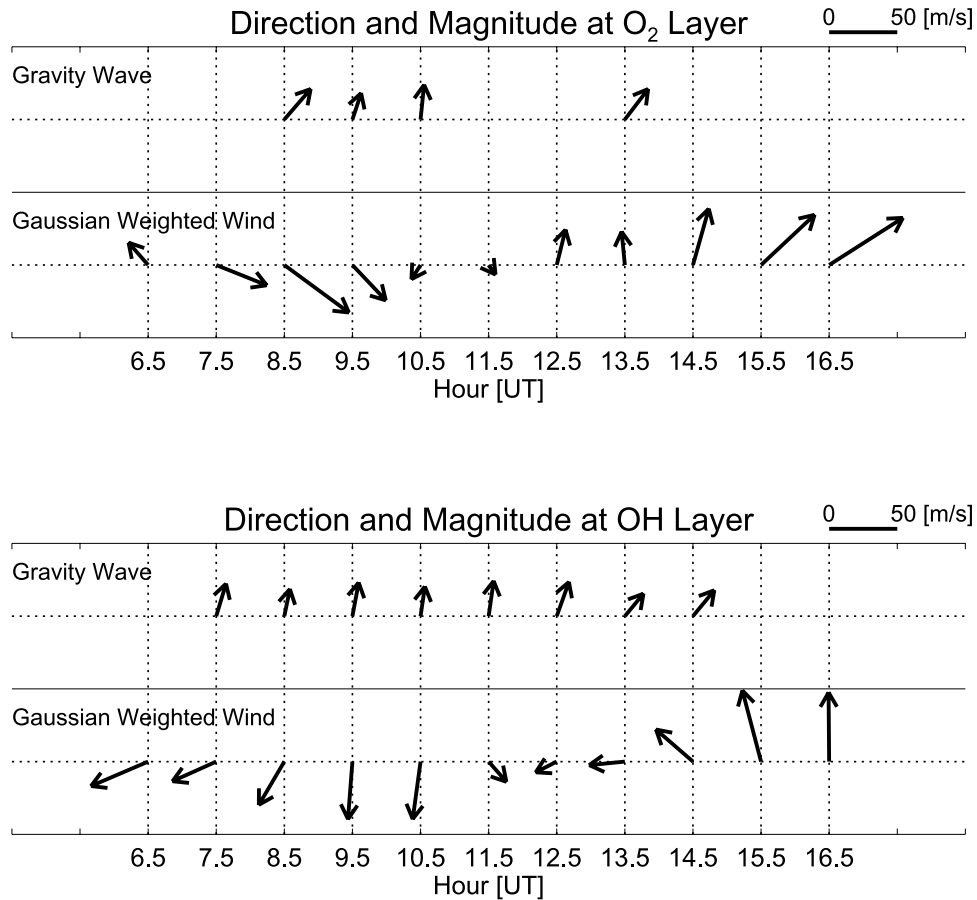
Figure 7. Arrows represent GW propagation hourly vectors (direction and speed) observed by the MTM and background wind measured by the MWR for 0600 to 1600 UT in the (bottom) OH and (top) O_2 layers on 29 June 2003. Vertical (horizontal) dotted lines mark the 0 m/s axis of zonal (meridional) winds. Up (right) is north (east). The vertical dotted line intervals and horizontal dotted and solid line intervals correspond to 50 m/s. No arrow is shown when GWs were absent in eight sequential images over 1 h.

[19] Temporal variations of the projected background wind (in the horizontal GW propagation direction) every 30 min for the O_2 (Figure 8, top) and OH (Figure 8, bottom) layers are shown. The projected background wind data are shown as black dots and by open circles when the GWs were absent. Gray dots depict when GWs were difficult to see in which case the propagation parameters could not easily be analyzed and have been estimated (see Figure 8 caption for more details). It is evident that the projected background wind at the O_2 layer nearly equaled the GW horizontal phase speed around 1400 UT, suggesting that a CL was generated. The projected background winds at the OH layer at 1430 UT and 1500 UT remained lower than the GW horizontal phase speed. The derived intrinsic phase speeds and vertical wavelengths of the GWs measured in the OH data are plotted in Figure 9 (top and middle) at 30-min intervals. The intrinsic phase speeds decreased with time from 63 m/s at 0930 UT to 25 m/s at 1430 UT. The vertical wavelengths also decreased with time, falling below the typical width of the OH layer (~10 km) around 1430 UT, indicating that the GW approached a CL, although the GW had not reached the CL when it disappeared.

[20] The momentum flux (F_M) of the GW evident in the OH data were calculated every 30 min and are also shown in

Figure 9 (bottom). For the first ~4.5 h the F_Ms were relatively low around 5 m^2/s^2, but after ~1130 UT they became significantly larger (with high uncertainties) and more variable. This sudden change (increase) in F_M was probably due to a decrease in the vertical group velocity of the wave associated with the marked decrease in its vertical wavelength (λ_z). The average values of all the calculated F_Ms are 13 m^2/s^2 for the OH data and 21 m^2/s^2 for the O_2 data (not shown). The intrinsic phase speed ($|c - u|$) represents an upper limit on the perturbation amplitude of horizontal velocity based on a convective instability threshold, $|u'|_{max} \sim |c - u|$ [*Fritts et al.*, 2002]. The $|u'|_{max}$ is GW saturation amplitude, and an altitude at which the GW horizontal perturbation becomes equal to $|u'|_{max}$ is the saturation level (SL). The $|u'|_{max}$ can be estimated using momentum flux ($F_M = (2|u'||w'|)^{-1}$) and the continuity equation, $k|u'| = -m|w'|$, assuming that F_M did not vary with altitude [*Fritts*, 1984].

[21] Figure 10 shows vertical profiles of the background wind and GW parameters ($c - u$ and $|u'|$) between 1345 and 1500 UT, around the time of the GW disappearances in the O_2 (Figures 10a and 10b) and OH (Figures 10c–10e) data. Each plot contains four profiles: ($c - u$) (black solid thick line) and $|u'|$ (black solid thin line) for the GWs, projected wind (u, gray broken line), and its increase in time (δu,
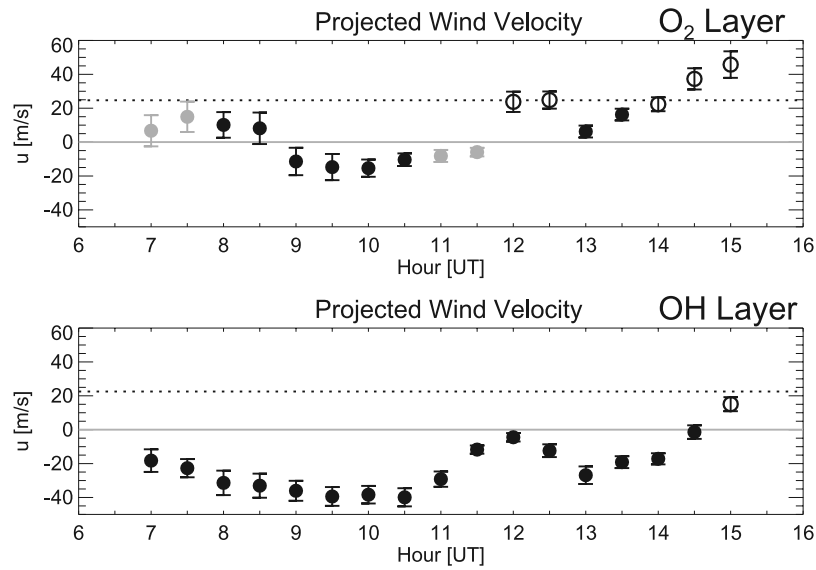
Figure 8. Projected wind temporal variations every 30 min at the (top) O_2 and (bottom) OH altitudes. Projected winds are shown as black dots, gray dots (when GWs were difficult to see, so that the propagation parameters could not be analyzed), and circles (when GWs were absent). The projected winds shown as gray dots and circles were calculated using the propagation directions of GWs observed at the previous UT. Those before 0800 UT for O_2 were calculated using the direction of GW observed at 0800 UT. Standard deviations of each value are shown as vertical error bars. Dotted lines show the nightly average of observed phase speeds.
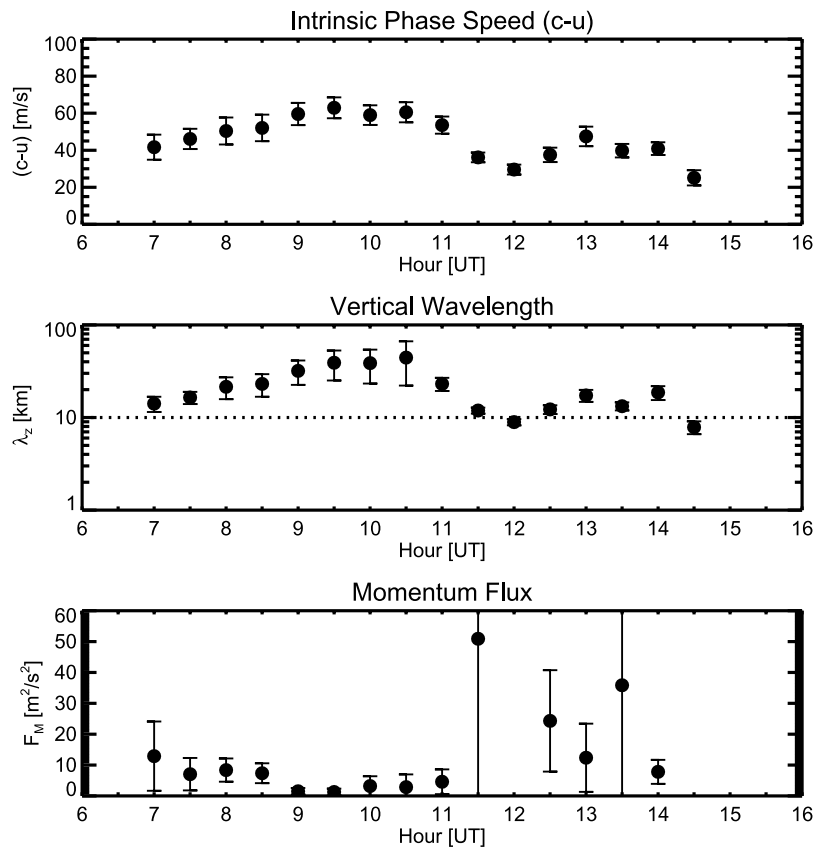

Figure 9. Temporal variations in the GW propagation parameters obtained at the OH layer: (top) horizontal intrinsic phase speeds ($c - u$), (middle) vertical wavelengths (λ_z), and (bottom) momentum flux (F_M). Vertical bars show standard deviation errors.
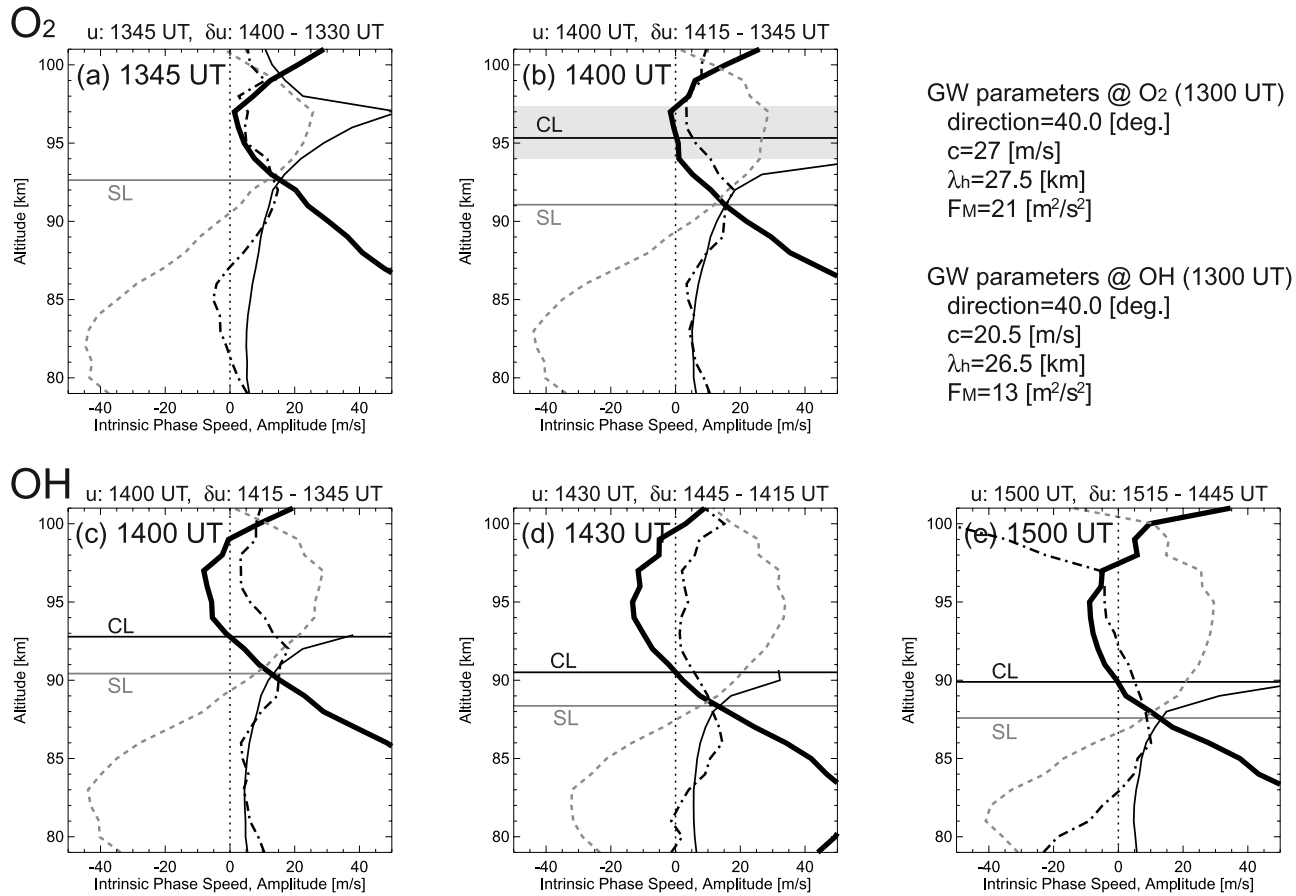
Figure 10. Relationships between critical levels (CL), saturation levels (SL), and background wind variations around the time of the GW disappearances in the (a, b) O_2 and (c, d, and e) OH layers. Each plot has four profiles: $(c - u)$ (black solid thick line) and $|u'|$ (black solid thin line) of the GWs, projected wind (u, gray dashed line), and 30-min difference of u (δu, black dash-dotted line); for example, $\delta u_{(1400UT)} = u_{(1415UT)} - u_{(1345UT)}$. The GW parameters observed at 1300 UT used for the profile calculations appear at top right.

black dash-dotted line). For example, δu at 1400 UT ($\delta u_{(1400UT)}$) was calculated as the 30-min difference of u, $\delta u_{(1400UT)} = u_{(1415UT)} - u_{(1345UT)}$, where u is the wind velocity at 30-min time resolution. In each plot, $|u'|$ and $(c - u)$ were calculated using the GW parameters at 1300 UT, for example, $\lambda_h = 27.5$ km (for the O_2) and 26.5 km (OH), $c = 27$ m/s (O_2) and 20.5 m/s (OH), and a propagation direction of 40 degrees.

[22] The GW observed in the O_2 data disappeared immediately around 1400 UT, as shown in Figure 4. Figure 10a indicates an SL in the O_2 data at 92.5 km around 1345 UT (before the GW disappearance), but no CL. However, a CL was generated around 94 to 97.5 km at 1400 UT, as depicted in Figure 10b. The CL altitudes coincided well with the typical peak emission altitude of the O_2 layer (~94 km). In the OH data, the GW horizontal wavelength became shorter at ~1430 UT before fading out (as shown in Figure 5). Figures 10c–10e show that although a CL existed, it was located above 90 km (even at 1500 UT after the GW disappearance), which was higher than the typical altitude of the OH layer (~87 km). These plots show that both the CL and SL moved down with a speed of ~3 km/h. Impor-

tantly, the SL was only ~1 km above the OH peak altitude at 1430 UT. This suggests that the GW disappearance in the OH data was not caused by a CL-GW interaction, but instead occurred at or below the SL. With the CL and SL descent, the GW λ_z decreased to less than 10 km at 1430 UT and may have broken down at the OH layer owing to the short λ_z. It is also possible that the small λ_z could have caused the fainter wave structure witnessed before the disappearance (due to cancellation effects within the OH layer). In contrast, the GW at the O_2 layer probably propagated very close to the CL at 1400 UT, as shown in Figures 10b and 10c. Thus, a probable cause for the GW disappearance is mainly a CL-GW interaction during which the GW may have saturated and lost some of its F_M before disappearing.

[23] To quantify the effects of the GW disappearances, δu (30-min difference of background wind) profiles are also displayed in Figure 10. When the GW in the O_2 data disappeared around 1400 UT (Figure 10b), δu was 5 to 10 m/s at the CL (94–97.5 km) and 15 m/s around 89 to 93 km (below the CL). The 90.5- to 93-km range marked a region between the SL and CL for the GW present in the OH data (Figure 10c). Impulses applied to background

wind (Δu) by the F_M of GWs were estimated using $\Delta u = F_M \Delta t / \Delta z$ [*Fritts et al.*, 2002], where Δt is the duration of wave breaking (saturation) and Δz is the height extent of the breaking (saturation) event. The GW in the O_2 data disappeared owing to a CL generated between 94 to 97.5 km (Δz = 3.5 km) within 15 min; Δt might be approximately 5 min, as the GW disappeared between two images obtained in a 5-min interval (Figure 5). The average F_M of the GW before disappearance (before 1400 UT) was 21 m^2/s^2; therefore, the expected Δu (by the GW disappearance) was ~5.5 m/s (Δt = 15 min) or less. As shown in Figure 10c, the SL and CL for the GW in the OH data occurred at 90.5 to 93 km (2.5 km width) at 1400 UT. The SL-CL region moved down with a speed of ~3 km/h and the average F_M of the GW before the break was 13 m^2/s^2. Therefore, Δu (by the GW saturation) was estimated at 9.5 m/s for 30 min (Δz = 2.5 km, Δt = 50 min). This value is somehow larger than the Δu of 5.5 m/s at the CL, but is qualitatively consistent with the δu profile at 1400 UT. When the GW in the OH data disappeared around 1430 UT, δu in Figure 10d increased over the 82 to 92 km range, with a maximum at 86 km, possibly occurring as a result of wave breaking with concurrent reduction in horizontal wavelength in the OH data. Additionally, the upper part (86–92 km) of the acceleration region was wider than the bottom part (82–86 km). This could have arisen from extra acceleration in the upper region from GW saturation between the SL and CL (88–90.5 km).

[23] The CL-GW interaction was probably triggered by a background wind change associated with the large-scale wave (period >10 h) observed on 29 June as shown in Figure 1. The perturbation may also have included vertically propagating semidiurnal and diurnal tides. However, the observed downward motion of the SL and CL (~3 km/h) was higher than the typical downward phase speed of the diurnal tide (~1 km/h). A single-mode diurnal tide cannot progress so quickly; we must take other effects into account, such as superposition of other waves (such as semidiurnal tides) and/or wind profile modification due to background wind acceleration by the breaking GW.

[25] Finally, the temporal variations in O_2 and OH rotational temperatures observed by the MTM showed no significant change between 1400 and 1500 UT. This differs from the ~40 K temperature increase reported by *Huang et al.* [1998, 2002] associated with a CL-GW interaction.

6. Conclusions

[26] On 29 June 2003, strong, diurnal oscillations were observed in both the zonal and meridional wind components over all measured altitudes (~80–100 km) by the Meteor Wind Radar (MWR) sited at Kihei, Maui, Hawaii, most probably dominated by large-scale GWs (period >10 h), which also include propagating semidiurnal and diurnal tides. On the same night, a short-period (~20-min) gravity wave (GW) was observed by a Mesospheric Temperature Mapper (MTM) located near the summit of Haleakala Crater, Maui, Hawaii. This GW was evident in both the OH and O_2 airglow layers for much of the night but disappeared around 1430 and 1400 UT, in each airglow layer, respectively. Qualitative and quantitative investigations into the relation-

ships between the observed GW dissipations and the increasing background wind field indicate the following:

[27] 1. The GW disappearance at the O_2 layer was most probably caused by a critical level gravity wave (CL-GW) interaction at the CL that occurred rapidly (within 15 min) around 1400 UT over the altitude ranges of ~94 to 97.5 km.

[28] 2. The GW disappearance at the OH layer was apparently not due to a CL-GW interaction. On the basis of the slow descent of the saturation level (SL) and the small intrinsic phase speed ($c - u$) at the OH layer altitude, the GW disappearance was probably caused by saturation and/or dissipations due to eddy diffusivity. The associated reduction in the vertical wavelength (λ_z) <10 km could also have contributed to the GW disappearance.

[29] 3. The wave disappearance may have accelerated the background wind, resulting in an increase of ~9.5 m/s for 30 min; however, coincident measurements of the background temperature did not reveal any accompanying change owing to the wave disappearance.

[30] 4. The acceleration at the CL around the O_2 layer was smaller than that below the CL because the CL descended rapidly and did not remain long there.

[31] Finally, it is important to note that dynamical and convective instabilities are the processes that alleviate the wave-breaking condition, but wave breaking at the CL and SL, as seen in this study, accelerated the background wind in the direction in which breaking occurs more easily, and at the lower altitudes, by creating a stronger wind shear. Wave breaking at the CL and SL is therefore an important process in long-period (>10 h) – short-period (<1 h) GW interactions. A major factor in clearing the wave breaking is considered to be the further phase progression of tides altering the wind shear direction.

References

Booker, J., and F. Bretherton (1967), The critical layer for internal gravity waves in a shear flow, *J. Fluid Mech.*, *27*, 513–539, doi:10.1017/S0022112067000515.

Breeding, R. J. (1971), A non-linear investigation of critical levels for internal atmospheric gravity waves, *J. Fluid Mech.*, *50*, 545–563, doi:10.1017/S0022112071002751.

Bretherton, F. P. (1966), The propagation of groups of internal gravity waves in a shear flow, *Q. J. R. Meteorol. Soc.*, *92*, 466–480, doi:10.1002/qj.49709239403.

Coble, M. R., G. C. Papen, and C. S. Gardner (1998), Computing two-dimensional unambiguous horizontal wavenumber spectra from OH airglow images, *IEEE Trans. Geosci. Remote Sens.*, *36*(2), 368–382, doi:10.1109/36.662723.

Ejiri, M. K., K. Shiokawa, T. Ogawa, K. Igarashi, T. Nakamura, and T. Tsuda (2003), Statistical study of short-period gravity waves in OH and OI nightglow images at two separated sites, *J. Geophys. Res.*, *108*(D21), 4679, doi:10.1029/2002JD002795.

Espy, P. J., G. O. L. Jones, G. R. Swenson, J. Tang, and M. J. Taylor (2004), Seasonal variations of the gravity wave momentum flux in the Antarctic mesosphere and lower thermosphere, *J. Geophys. Res.*, *109*, D23109, doi:10.1029/2003JD004446.

Franke, S. J., X. Chu, A. Z. Liu, and W. K. Hocking (2005), Comparison of meteor radar and Na Doppler lidar measurements of winds in the meso-

pause region above Maui, Hawaii, *J. Geophys. Res.*, *110*, D09S02, doi:10.1029/2003JD004486.

Fritts, D. C. (1984), Gravity wave saturation in the middle atmosphere: A review of theory and observations, *Rev. Geophys.*, *22*, 275–308, doi:10.1029/RG022i003p00275.

Fritts, D. C., and R. A. Vincent (1987), Mesospheric momentum flux studies at Adelaide, Australia: Observations and a gravity wave/tidal interaction model, *J. Atmos. Sci.*, *44*, 605–619, doi:10.1175/1520-0469(1987)044<0605:MMFSAA>2.0.CO;2.

Fritts, D. C., J. R. Isler, J. H. Hecht, R. L. Walterscheid, and Ø. Andreassen (1997), Wave breaking signatures in sodium densities and OH nightglow: 2. Simulation of wave and instability structures, *J. Geophys. Res.*, *102*(D6), 6669–6684, doi:10.1029/96JD01902.

Fritts, D. C., S. L. Vadas, and Y. Yamada (2002), An estimate of strong local body forcing and gravity wave radiation based on OH airglow and meteor radar observations, *Geophys. Res. Lett.*, *29*(10), 1429, doi:10.1029/2001GL013753.

Garcia, F. J., M. J. Taylor, and M. C. Kelley (1997), Two-dimensional spectral analysis of mesospheric airglow image data, *Appl. Opt.*, *36*(29), 7374–7385, doi:10.1364/AO.36.007374.

Gardner, C., and M. J. Taylor (1998), Observational limits for lidar, radar, and airglow imager measurements of gravity wave parameters, *J. Geophys. Res.*, *103*(D6), 6427–6437, doi:10.1029/97JD03378.

Gardner, C. S., K. Gulati, Y. Zhao, and G. R. Swenson (1999), Measuring gravity wave momentum fluxes with airglow images, *J. Geophys. Res.*, *104*(D10), 11,903–11,915.

Gavrilov, N. M., et al. (1995), Climatological monthly characteristics of middle atmosphere gravity waves (10-min 10-h) during 1979–1993 at Saskatoon, *Ann. Geophys.*, *13*(3), 285–295.

Gossard, E. E., and W. H. Hooke (1975), *Wave in the Atmosphere*, Elsevier, New York.

Hazel, P. (1967), The effect of viscosity and heat conduction on internal gravity waves at a critical level, *J. Fluid Mech.*, *30*, 775–786, doi:10.1017/S0022112067001752.

Hecht, J. H., et al. (1993), Simultaneous nightglow and Na lidar observations at Arecibo during the AIDA-89 campaign, *J. Atmos. Terr. Phys.*, *55*, 409–423, doi:10.1016/0021-9169(93)90077-C.

Hecht, J. H., R. L. Walterscheid, D. C. Fritts, J. R. Isler, D. C. Senft, C. S. Gardner, and S. J. Franke (1997), Wave breaking signatures in OH airglow and sodium densities and temperature: 1. Airglow imaging, Na lidar, and MF radar observations, *J. Geophys. Res.*, *102*(D6), 6655–6668, doi:10.1029/96JD02619.

Hecht, J. H., C. Fricke-Begemann, R. L. Walterscheid, and J. Höffner (2000), Observations of the breakdown of an atmospheric gravity wave near the cold summer mesopause at 54°N, *Geophys. Res. Lett.*, *27*(6), 879–882.

Hecht, J. H., R. L. Walterscheid, and R. A. Vincent (2001), Airglow observations of dynamical (windshear-induced) instabilities over Adelaide, Australia, associated with atmospheric gravity waves, *J. Geophys. Res.*, *106*(D22), 28,189–28,197, doi:10.1029/2001JD000419.

Hickey, M. P., and J. S. Brown (2002), A simulation study of space-based observations of gravity waves in the airglow using observed ALOHA-93 wave parameters, *J. Geophys. Res.*, *107*(A12), 1431, doi:10.1029/2001JA009225.

Hines, C. O. (1960), Internal atmospheric gravity waves at ionospheric heights, *Can. J. Phys.*, *38*(11), 1441–1481.

Hines, C. O. (1968), Some consequences of gravity-wave critical layers in the upper atmosphere, *J. Atmos. Terr. Phys.*, *30*, 837–843.

Hocking, W. K., and T. Thayaparan (1997), Simultaneous and co-located observation of winds and tides by MF and meteor radars over London, Canada (43°N, 81°W), during 1994–1996, *Radio Sci.*, *32*(2), 833–865, doi:10.1029/96RS03467.

Huang, T. Y., H. Hur, T. F. Tuan, X. Li, E. M. Dewan, and R. H. Picard (1998), Sudden narrow temperature-inversion-layer formation in ALOHA-93 as a critical-layer-interaction phenomenon, *J. Geophys. Res.*, *103*(D6), 6323–6332, doi:10.1029/97JD03076.

Huang, T.-Y., M. P. Hickey, T.-F. Tuan, E. M. Dewan, and R. H. Picard (2002), Further investigations of a mesospheric inversion layer observed in the ALOHA-93 Campaign, *J. Geophys. Res.*, *107*(D19), 4408, doi:10.1029/2001JD001186.

Lindzen, R. S. (1981), Turbulence and stress owing to gravity wave and tidal breakdown, *J. Geophys. Res.*, *86*(C10), 9707–9714, doi:10.1029/JC086iC10p09707.

Lloyd, K. H., C. H. Low, and R. A. Vincent (1973), Turbulence, billows, and gravity waves in a high shear region of the upper atmosphere, *Planet. Space Sci.*, *21*, 653–661, doi:10.1016/0032-0633(73)90076-7.

Meek, C. E., and A. H. Manson (1992), Angle-of-arrival oscillations in the mesosphere as seen by medium frequency (MF) radar, *J. Atmos. Terr. Phys.*, *54*, 277–293, doi:10.1016/0021-9169(92)90008-9.

Meriwether, J. W. (1984), Ground based measurements of mesospheric temperatures by optical means, in *Middle Atmosphere Program Handbook for MAP*, vol. 13, edited by R. Vincent, pp. 1–18, NASA Goddard Space Flight Center, Greenbelt, Md.

Nakamura, T., T. Tsuda, M. Yamamoto, S. Fukao, and S. Kato (1993), Characteristics of gravity waves in the mesosphere observed with the MU radar: 1. Momentum flux, *J. Geophys. Res.*, *98*(D5), 8899–8910, doi:10.1029/92JD02978.

Nakamura, T., A. Higashikawa, T. Tsuda, and Y. Matsushita (1999), Seasonal variations of gravity wave structures in OH airglow with a CCD imager at Shigaraki, *Earth Planets Space*, *51*, 897–906.

Nakamura, T., T. Tsuda, R. Maekawa, M. Tsutsumi, K. Shiokawa, and T. Ogawa (2001), Seasonal variation of gravity waves with various temporal and horizontal scales in the MLT region observed with radar and airglow imaging, *Adv. Space Res.*, *27*, 1737–1742, doi:10.1016/S0273-1177(01)00310-6.

Nakamura, T., T. Aopno, T. Tsuda, A. G. Admiranto, E. Achmad, and Suranto (2003), Mesospheric gravity waves over a tropical convective region observed by OH airglow imaging in Indonesia, *Geophys. Res. Lett.*, *30*(17), 1882, doi:10.1029/2003GL017619.

Pendleton, W. R., Jr., M. J. Taylor, and L. C. Gardner (2000), Terdiurnal oscillations in OH Meinel rotational temperatures for fall conditions at northern midlatitude sites, *Geophys. Res. Lett.*, *27*(12), 1799–1802, doi:10.1029/2000GL003744.

Reid, I. M. (1986), Gravity wave motions in the upper middle atmosphere (60–110 km), *J. Atmos. Terr. Phys.*, *48*, 1057–1072, doi:10.1016/0021-9169(86)90026-7.

Reid, I. M., R. Rüster, and G. Schmidt (1987), VHF radar observations of cat's-eye-like structures at mesospheric heights, *Nature*, *327*, 43–45, doi:10.1038/327043a0.

She, C. Y., J. R. Yu, J. W. Huang, C. Nagasawa, and C. S. Gardner (1991), Na temperature lidar measurements of gravity wave perturbations of wind, density and temperature in the mesopause region, *Geophys. Res. Lett.*, *18*(7), 1329–1331, doi:10.1029/91GL01517.

Suzuki, S., K. Shiokawa, Y. Otsuka, T. Ogawa, and P. Wilkinson (2004), Statistical characteristics of gravity waves observed by an all-sky imager at Darwin, Australia, *J. Geophys. Res.*, *109*, D20S07, doi:10.1029/2003JD004336.

Suzuki, S., K. Shiokawa, Y. Otsuka, T. Ogawa, K. Nakamura, and T. Nakamura (2007), A concentric gravity wave structure in the mesospheric airglow images, *J. Geophys. Res.*, *112*, D02102, doi:10.1029/2005JD006558.

Swenson, G. R., and A. Z. Liu (1998), A model for calculating acoustic gravity wave energy and momentum flux in the mesosphere from OH airglow, *Geophys. Res. Lett.*, *25*(4), 477–480, doi:10.1029/98GL00132.

Swenson, G. R., M. J. Taylor, P. J. Espy, C. Gardner, and X. Tac (1995), ALOHA-93 measurements of intrinsic AGW characteristics using airborne airglow imager and groundbased NA wind/temperature lidar, *Geophys. Res. Lett.*, *22*(20), 2841–2844.

Tang, J., A. Z. Liu, and G. R. Swenson (2002), High frequency gravity waves observed in OH airglow at Starfire Optical Range, NM: Seasonal variations in momentum flux, *Geophys. Res. Lett.*, *29*(20), 1966, doi:10.1029/2002GL015794.

Tang, J., G. R. Swenson, A. Z. Liu, and F. Kamalabadi (2005), Observational investigations of gravity wave momentum flux with spectroscopic imaging, *J. Geophys. Res.*, *110*, D09S09, doi:10.1029/2004JD004778.

Tao, X., and C. S. Gardner (1995), Heat flux observations in the mesopause region above Haleakala, *Geophys. Res. Lett.*, *22*(20), 2829–2832.

Taylor, M. J., E. H. Ryan, T. F. Tuan, and R. Edwards (1993), Evidence of preferential directions for gravity wave propagation due to wind filtering in the middle atmosphere, *J. Geophys. Res.*, *98*(A4), 6047–6057, doi:10.1029/92JA02604.

Taylor, M. J., W. R. Pendleton Jr., S. Clark, H. Takahashi, D. Gobbi, and R. A. Goldberg (1997), Image measurements of short-period gravity waves at equatorial latitudes, *J. Geophys. Res.*, *102*(D22), 26,283–26,299.

Taylor, M. J., W. R. Pendleton Jr., H.-L. Liu, C. Y. She, L. C. Gardner, R. G. Roble, and V. Vasoli (2001), Large amplitude perturbations in mesospheric OH Meinel and 87-km Na lidar temperatures around the autumnal equinox, *Geophys. Res. Lett.*, *28*(9), 1899–1902, doi:10.1029/2000GL012682.

Vargas, F., G. Swenson, A. Liu, and D. Gobbi (2007), O(^{1}S), OH, and O$_2$(A) airglow layer perturbations due to AGWs, and their implied effects on the atmosphere, *J. Geophys. Res.*, *112*, D14102, doi:10.1029/2006JD007642.

Vincent, R. A. (1984), Gravity-wave motions in the mesosphere, *J. Atmos. Terr. Phys.*, *46*, 119–128, doi:10.1016/0021-9169(84)90137-5.

Walterscheid, R. L., J. H. Hecht, R. A. Vincent, I. M. Reid, J. Woithe, and M. P. Hickey (1999), Analysis and interpretation of airglow and radar observations of quasi-monochromatic gravity waves in the upper meso-

sphere and lower thermosphere over Adelaide, Australia (35°S, 138°E), *J. Atmos. Terr. Phys.*, *61*, 461–478, doi:10.1016/S1364-6826(99)00002-4.

Wrasse, C. M., et al. (2006), Reverse ray tracing of the mesospheric gravity waves observed at 23°S (Brazil) and 7°S (Indonesia) in airglow imagers, *J. Atmos. Terr. Phys.*, *68*, 163–181, doi:10.1016/j.jastp.2005.10.012.

Wu, Q., and T. L. Killeen (1996), Seasonal dependence of mesospheric gravity waves (<100 km) at Peach Mountain Observatory, Michigan, *Geophys. Res. Lett.*, *23*(17), 2211–2214, doi:10.1029/96GL02168.

Yamada, Y., H. Fukunishi, T. Nakamura, and T. Tsuda (2001), Breaking of small-scale gravity wave and transition to turbulence observed in OH airglow, *Geophys. Res. Lett.*, *28*(11), 2153–2156, doi:10.1029/2000GL011945.

Zhao, Y., M. J. Taylor, and X. Chu (2005), Comparison of simultaneous Na lidar and mesospheric nightglow temperature measurements and the effects of tides on the emission layer heights, *J. Geophys. Res.*, *110*, D09S07, doi:10.1029/2004JD005115.

————————————

M. K. Ejiri and T. Nakamura, Research Institute for Sustainable Humanosphere, Kyoto University, Gokasho, Uji, Kyoto 611-0011, Japan. (mitsumu@rish.kyoto-u.ac.jp)

S. J. Franke, Department of Electrical and Computer Engineering, University of Illinois at Urbana-Champaign, 320 CSL, 1308 West Main Street, Urbana, IL 61801, USA.

M. J. Taylor, Center for Atmospheric and Space Sciences, Utah State University, 4405 Old Main Hill, SER Building, Logan, UT 84322-4405, USA.